

Research Article

Nondestructive Testing of Metallic Cables Based on a Homogenized Model and Global Measurements

Valdemar Melicher¹ and Peter Sergeant^{2,3}

¹ *Research Group for Numerical Analysis and Mathematical Modelling,
Department of Mathematical Analysis, Galglaan 2, 9000 Gent, Belgium*

² *Department of Electrical Energy, Systems and Automation, Ghent University, Sint-Pietersnieuwstraat 41,
9000 Gent, Belgium*

³ *Department of Electrotechnology, Faculty of Applied Engineering Sciences, University College Ghent,
Schoonmeersstraat 52, 9000 Gent, Belgium*

Correspondence should be addressed to Valdemar Melicher, valdemar.melicher@ugent.be

Received 16 July 2010; Revised 21 October 2010; Accepted 21 December 2010

Academic Editor: Dane Quinn

Copyright © 2010 V. Melicher and P. Sergeant. This is an open access article distributed under the Creative Commons Attribution License, which permits unrestricted use, distribution, and reproduction in any medium, provided the original work is properly cited.

We propose a simple, quick, and cost-effective method for nondestructive eddy-current testing of metallic cables. Inclusions in the cross section of the cable are detected on the basis of certain global data: hysteresis loop measurements for different frequencies. We detect air-gap inclusions inside the cross section using a homogenized model. The problem, which can be understood as an inverse spectral problem, is posed in two dimensions. We consider its reduction to one dimension. The identifiability is studied. We obtain a uniqueness result for a single inclusion in 1D by two measurements for sufficiently low frequency. We study the sensibility of the inverse problem numerically. A study case with real data is performed to confirm the usefulness.

1. Introduction

In [1], a homogenized model is derived for nondestructive testing (NDT) of heterogeneous magnetic structures (cables). In this contribution, we employ the model for actual NDT.

NDT can be based on eddy currents or on magnetic properties.

In case of eddy current testing, the imposed field has a sufficiently high frequency so that eddy currents are induced in the device under test. Cracks can be detected because they change the path of the eddy currents. The frequency of the excitation determines—via the penetration depth—the thickness of the scanned region: in case of high frequencies, mainly the surface is scanned; in case of lower frequencies, also cracks deeper inside the material will be detected. The paper [2] explains the principle of eddy current sensors and investigates the

effect of inhomogeneity of the target material. In [3, 4], computational techniques are given to solve the magnetic field problem in eddy current testing. Both papers also present eddy current testing experiments: Cardelli et al. consider benchmark problems of an aluminium plate with different cylindrical defects; Li et al. apply the eddy current testing technique to multilayer conductive structures.

In case of NDT based on magnetic properties, there are techniques that exploit the magnetic reluctance variation and techniques that measure magnetic flux leakage. Here, the frequency of excitation can be very low; even excitation with permanent magnets is possible. In [5, 6], these two techniques for magnetic analysis of NDT are studied for ferromagnetic ropes. The cable is modelled in a 3D numerical model as one solid object with uniform properties. The individual strands are not modelled and—as the magnetic NDT in the cited paper is static—the considered static numerical model has no eddy currents.

The model of the ferromagnetic cable that we derived in [1] is useful for NDT of cables, both for excitation at low frequency (where changes in magnetic properties are investigated) and at higher frequency (eddy current testing). It is valid for a wide range of amplitudes and frequencies.

The motivation of the work in this paper is to improve the performance of nondestructive testing techniques by exploiting information in the magnetic behaviour of the target material. We show that by solving an inverse problem based on the model and on measured hysteresis loops at several frequencies a broader range of defects in the cable can be detected.

In Section 1.2, we recall shortly the model derived in [1]. In Section 2, we introduce the problem we study, which can be classified as a 2D inverse spectral problem. We consider its reduction to 1D. Subsequently in Section 3 we study an inverse problem using the 1D model. It results in a simple two-parameter determination problem. We validate the method in a real data experiment in Section 4.

1.1. Detection Setup

Let us have a heterogeneous cable consisting of many thin strands. Usually, the strands are not isolated separately. A coating can be applied to the cable to avoid corrosion. We consider NDT of such a cable based on magnetic hysteresis and eddy currents. The detector has a very simple design. It is made of a single excitation coil and a single measurement coil, which are wound around the cable, see Figure 1. When an alternating current flows through the induction coil, the corresponding alternating magnetic field is induced. Consequently, eddy currents are induced in the cable.

Due to the heterogeneous nature of the problem, very fine space discretizations, for example, very fine meshes for finite element models (FEM), are required to obtain a feasible accuracy of a model. A certain model reduction has to be applied to avoid extensive computational costs.

1.2. Model

The facts presented in this section are direct consequences of the results obtained in [1].

Let the circular cross section of a cable be the computational domain Ω . The outer circular boundary of Ω is denoted by Γ_E . We introduce into the cable an inclusion Ω_I . For a multiplicity of exposition, we assume that Ω_I is simply connected, that is, that we have only

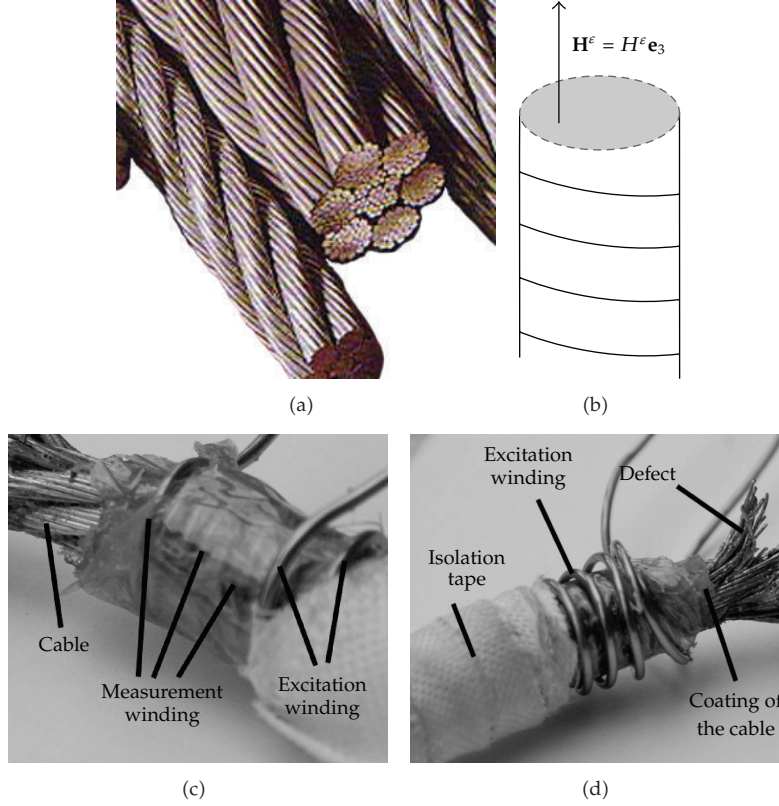


Figure 1: (a) uncoated cable with 7 bundles of strands, (b) 2D scalar model, (c) experimental setup: a part of the excitation and the measurement winding around the coated cable. The coating is removed on the left of the figure to clearly show the individual strands, (d) cable where one bundle of strands is removed over a length of 1 cm. To make the defect visible, the coating is removed and the “defect” bundle of strands is folded in radial direction. Evidently, the method for NDT does not require the defect to be visible.

one inclusion. Ω_I is filled with nonconductive material (air), that is, $\sigma = 0$. The boundary of Ω_I is denoted by Γ_I . Let us define $\Gamma := \Gamma_E \cup \Gamma_I$ and $\Omega_C := \Omega \setminus \overline{\Omega_I}$. We suppose that Ω_C is filled with a conductive material (metal). Further, we assume that the inclusion is buried inside, that is, $\text{dist}(\Omega_I, \Gamma_E) > 0$ ($\Gamma_E \cap \Gamma_I = \emptyset$). Otherwise it could be detectable by visual inspection, see Figure 2.

If the induction coil is sufficiently uniform, it induces the magnetic field \mathbf{H} perpendicular to the cross section of the cable. Let $\mathbf{e}_1, \mathbf{e}_2, \mathbf{e}_3$ be the Cartesian coordinate system and let an infinitely long cable be aligned along \mathbf{e}_3 . We have

$$\mathbf{H} = H\mathbf{e}_3. \quad (1.1)$$

In [1], we assumed that the diffusion of electromagnetic fields in the heterogeneous cable can be described by the Maxwell equations with periodically oscillating coefficients. An accurate and computationally efficient model can be then derived. The idea behind is to replace the heterogeneous material in the cross section by a fictitious homogeneous one, whose behaviour at the macroscopic level is a good approximation of the one of the composite

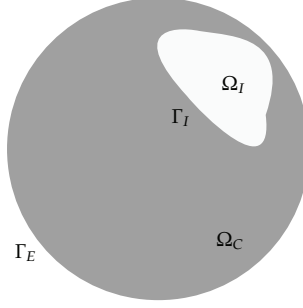


Figure 2: Problem setting.

material. We obtained such a homogenized (asymptotic) model employing the two-scale convergence. We validated the model on real steel cable data. In the isotropic case the model reads in the terms of H :

$$-\Delta H + i\omega\sigma^h\mu^h H = 0, \quad \text{in } \Omega_C, \quad (1.2)$$

$$H = H_E, \quad \text{on } \Gamma_E, \quad (1.3)$$

$$H - H_I = 0, \quad \text{on } \Gamma_I, \quad (1.4)$$

$$i\omega\sigma^h\mu_0|\Omega_I|H_I + \int_{\Gamma_I} \nabla H \cdot \mathbf{n} = 0, \quad (1.5)$$

where μ_0 is the permeability of the vacuum, ω is the angular frequency in rad/s, \mathbf{n} is the normal outer unit vector with respect to Ω_C and H_E is the prescribed Dirichlet boundary condition on the exterior boundary Γ_E . H_I is an a priori unknown boundary condition on the cavity (interior) boundary Γ_I . From physical reasons H_I is a complex and H_E a real constant. (1.5) is a nonlocal boundary condition on Γ_I obtained considering Ampère's law in Ω_C and the Faraday's law in Ω_I and using the continuity of tangential components of the electric and magnetic field intensities, together with the fact that the conductivity is zero in Ω_I . This extra condition is sufficient to determine H_I .

The homogenized conductivity σ^h and homogenized permeability μ^h are scalar, generally complex, constants. They are given by certain integral expressions on Y , the so-called Y -cell, from repetition of which Ω_C is made. Let us recall here, that, we assume that the heterogeneous cable has a periodic structure. For details, see [1]. Let us remark that σ^h is a scalar only in the isotropic case.

The homogenized system has an identical form as the original multiscale system. More importantly, we obtain exactly the system (1.2)–(1.5) if we consider a homogeneous cable made from a material with the permeability μ^h and the conductivity σ^h , that is, μ^h and σ^h preserve their physical interpretation. Consequently, the results we obtain in this paper are valid for the homogeneous case as well.

If the periodic permeability and the conductivity are bounded and coercive, the homogenized μ^h , σ^h are bounded and coercive as well. We obtain a unique solution $H \in H^1(\Omega_C)$ to (1.2)–(1.5), see [1].

We define the permeability in Ω by

$$\mu = \begin{cases} \mu^h, & \text{in } \Omega_C, \\ \mu_0, & \text{in } \Omega_I, \end{cases} \quad (1.6)$$

where μ_0 is the vacuum permeability, and the conductivity by

$$\sigma = \begin{cases} \sigma^h, & \text{in } \Omega_C, \\ 0, & \text{in } \Omega_I. \end{cases} \quad (1.7)$$

2. Inverse Spectral Problem

In this section, we study the problem of detection of inclusions buried inside the circular cross section of the cable as described in Section 1.2. We want to acquire as much information as possible about the inclusions based on the measurement for different frequencies.

The problem is closely related to the inverse conductivity problem [7], where one wants to determine an inclusion Ω_I , that is, the characteristic function χ_{Ω_I} , on the basis of Dirichlet-to-Neuman data on Γ_E . Let us prescribe certain Dirichlet boundary condition on Γ_E and then let us solve the governing (elliptic) equation. We can take the Neuman trace of the solution, if this one is regular enough. In this way we define the so-called Dirichlet-to-Neuman operator. The inverse conductivity problem lies in determining inclusions on the basis of one pair or more pairs of the corresponding Dirichlet-to-Neuman data. This problem is well studied, particularly in two-dimensions, see [7, 8] and references therein. In [8] the authors obtain uniqueness results in 2D for convex polygonal inclusions by two measurements.

Using the Dirichlet-to-Neuman approach for NDT of cables has two disadvantages. First, it is quite expensive to obtain local measurements of the magnetic field and the induction on Γ_E : it requires to build quite complicated sensors for local magnetic field and induction measurements [9], and the gathering of the measurements is a fairly slow process. However, it is the only way to obtain full topological information, that is, the support of an inclusion. Sometimes such a complete information is redundant, for example, it can only be important how big the inclusion is and how deep it is buried inside the cable. The second disadvantage of the Dirichlet-to-Neuman approach is that it does not exploit symmetry.

Let the macroscopic electromagnetic behaviour be described by (1.2)–(1.5), that is, the homogenized model which was validated in [1]. We can define to the solution H to (1.2)–(1.5) the corresponding operator \mathcal{H} which maps to ω and Ω_I this solution, that is, $\mathcal{H}(\omega, \Omega_I) : \mathbb{R} \times \tau \rightarrow H^1(\Omega)$, where τ is a certain topological space.

We cannot reach the solution H directly, we can only measure some global quantity dependent on H , for example, the magnetic energy. Consequently, we consider a certain functional $F(\mathcal{H}(\omega, \Omega_I)) : \mathbb{R} \times \tau \rightarrow \mathbb{C}$. The question is *what information can be obtained over Ω_I from the range $R(F)$ of functional F for $\omega \in [0, \infty)$* . This question is very general and vague. The answer is certainly dependent on functional F , topological restrictions of τ and the governing equation.

We categorize the problem as an *inverse spectral problem* (ISP) [7]. The question which ISP asks is if a domain Ω can be determined by the eigenvalues λ (resonance frequencies) of

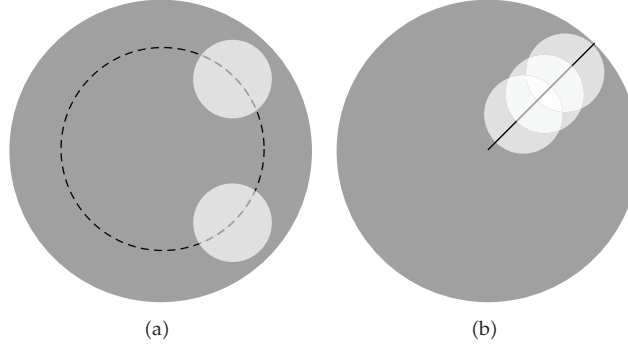


Figure 3: What can be determined?

an elliptic PDE with a homogeneous Dirichlet boundary condition on $\partial\Omega$. The problem, we study does not strictly belong to this category. We do not consider only the eigenvalues but $\omega \in [0, \infty)$. We do not try to recover the domain Ω itself, but only its inclusion Ω_I . Also the boundary conditions are nonhomogeneous, and the solution has to fulfill (1.5). The data are not the eigenvalues but certain global measurements $F(\mathcal{H}(\omega, \Omega_I))$. But the main goal is the same: to determine the geometry based on measurements for different frequencies.

2.1. Reduction of the Model to 1D

We will not solve the problem in two dimensions, but we will exploit the symmetry of the circular cross section and obtain a one-dimensional problem in radial direction. The reduction will be quite accurate. We will show numerically, that almost all the 2D spectral information can be described by the resulting 1D model.

Let us assume that the total magnetic flux through the cross section

$$F(\omega, \Omega_I) := \int_{\Omega} \mu H \quad (2.1)$$

is the global information available. This is one of the reasonable and physically relevant choices. Another one is the total magnetic energy inside the cross section.

First, the volume of the inclusion $|\Omega_I|$ is uniquely determined by a single measurement for $\omega = 0$. Then $H = H_E$ is the unique solution to (1.2)–(1.5). The permeability inside Ω_I is μ_0 and $\mu = \mu^h \neq \mu_0$ in Ω_C . Consequently, $|\Omega_I|$ is indeed determined by $F(0, \Omega_I)$. (It is not possible to obtain measurements for $\omega = 0$. By measurements for $\omega = 0$, we mean measurements for sufficiently low frequency.)

Second, since we hold a constant magnetic field H_E on Γ_E , we cannot distinguish two identical inclusions with different angular positions buried at the same radial position (depth), see Figure 3(a).

Third, the penetration depth of the magnetic field decreases if ω increases. Intuitively, inclusions deep inside can be identified based on low-frequency measurements. Inclusions close to Γ_E will alter $F(\omega, \Omega_I)$ also for high ω .

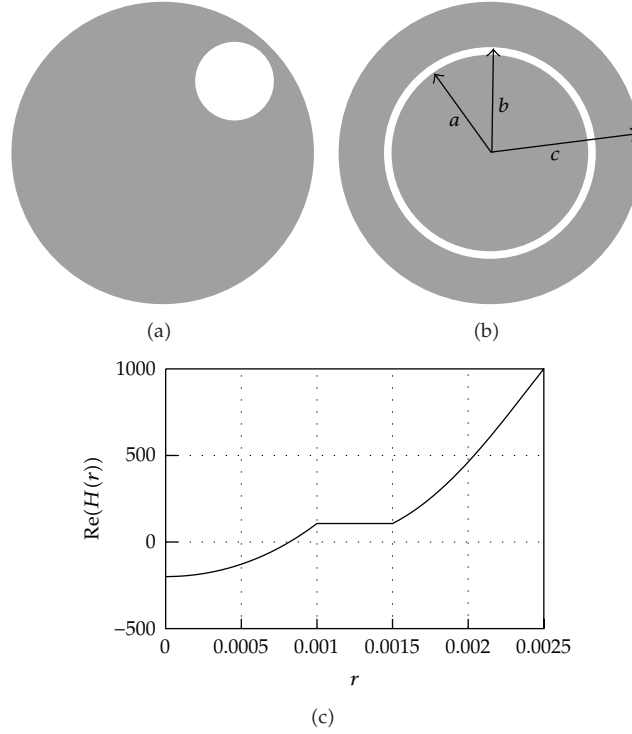


Figure 4: Symmetrization of inclusion: (a) the inclusion, (b) its symmetrization, and (c) $\text{Re}(H(r))$.

Based on the above heuristic, only the distribution of the “mass” along the radial direction is important. It seems, that there should exist a 1D model, which approximates the 2D case quite accurately.

We employ a simple idea to replace Ω_I by an auxiliary radial symmetric inclusion—a ring R_I , see Figure 4. Let a be the inner and b be the outer diameter of the ring inclusion. We ask $|\Omega_I| = |R_I|$ to be able to copy the case $\omega = 0$ and that the mass is buried at the same depth. The physical properties of R_I , that is, $\sigma = 0$, $\mu = \mu_0$ are the same as for Ω_I , that is, we replace Ω_I by an isolating ring. In such a way, Ω_I is described by only two-parameters, its surface and its depth, that is, the diameter of the ring $s = (a + b)/2$.

Another possible approach is to try to derive a model based on averaged physical properties along the radial direction. One could integrate the governing equations in polar coordinates, make some simplifying assumptions on the solution $H(r, \theta)$ (as $(\partial H(r, \theta)/\partial \theta) = 0$), and attempt to derive an approximative model using only averages in angular direction. The approach we use is more simple and illustrative.

Equation (1.2) in polar coordinates reads

$$-\frac{1}{r} \frac{\partial H}{\partial r} - \frac{\partial^2 H}{\partial r^2} - \frac{1}{r^2} \frac{\partial^2 H}{\partial \theta^2} + i\omega\mu^h \sigma^h H = 0. \quad (2.2)$$

Recalling that we have constant Dirichlet boundary condition $H = H_E$ on Γ_E and that the geometry is as depicted in Figure 4(b) we immediately argue that H is function of r only. Let

c be the radius of Ω and let $R_I = \{(r, \theta) \mid a < r < b, 0 < \theta \leq 2\pi\}$. Then (1.2)–(1.5) becomes

$$\frac{1}{r} \frac{dH}{dr} + \frac{d^2H}{dr^2} \forall \equiv \times = i\omega\sigma^h \mu^h H, \quad \text{in } \Omega_C, \quad (2.3)$$

$$H(c) = H_E, \quad (2.4)$$

$$H(a) = H(b) = H_I, \quad (2.5)$$

$$\frac{dH}{dr}(0) = 0, \quad (2.6)$$

$$i\omega\mu_0\sigma^h(b^2 - a^2)H_I = 2 \left[b \frac{dH(b^+)}{dr} - a \frac{dH(a^-)}{dr} \right]. \quad (2.7)$$

The solution of (2.3)–(2.7), depicted for $a = 0.001$ m, $b = 0.0015$ m, $c = 0.0025$ m, $\sigma^h = 4.1e6$ S/m, $\mu^h = 100\mu_0$, $H_E = 1000$ A/m (physical example) in Figure 4(c), can be computed explicitly. Let us define $k := \sqrt{-i\omega\mu^h\sigma^h}$. We obtain

$$H(r) = \begin{cases} c_1 J_0(kr), & r \in [0, a), \\ c_1 J_0(ka), & r \in [a, b), \\ c_2 J_0(kr) + c_3 K_0(-ikr), & r \in [b, c], \end{cases} \quad (2.8)$$

where J_0 is the Bessel function of the first kind of order 0 and K_0 is the modified Bessel function of the second kind of order 0. Condition (2.6) was used to rule out the fundamental solution K_0 on interval $[0, a)$, since $(d/dz)K_0(z) = -K_1(z)$ and $K_1(z)$ has a singularity in $z = 0$. The constants c_1 , c_2 , and c_3 are determined from (2.4) and (2.5). In (2.5), H_I is determined from (2.7), see the proof of Theorem 3.1 in Section 3.1.

Now, we compare numerically how well the 1D model (2.3)–(2.7) approximates the results of the 2D model for different inclusions Ω_I from the point of view of $F(H(\omega, \Omega_I))$. Real measurements, which are at least two-dimensional, have to be reproducible by the model. Good approximative properties are very important.

The 2D problem is solved by the finite element method. A very fine mesh is used, thus the solution is quasiprecise. To solve the resulting linear problem, a Cholesky solver with accuracy $\epsilon = 10^{-12}$ is employed. $F(\omega, \Omega_I)$ for $\omega = 2\pi 2^i$, $i = 1, \dots, 14$ is computed. We compare the resulting $F(\omega, \Omega_I)$ with the corresponding results of 1D model with the ring inclusion, that is, $F(\omega, R_I)$. First, let Ω_I to be a circular inclusion. This case is the most probable in real world applications. It represents a single strand of a cable. Figure 5 shows that visually the results of 1D and 2D model are indistinguishable. The relative error of $F(\omega, \Omega_I)$ is only 0.724%. Let us note, that the parameters a , b , c , H_E , σ^h and μ^h are here the same as by Figure 4(c), see the corresponding text above.

In Figure 6, there are results for square and box inclusions. For the square inclusion, the relative error of $F(\omega, \Omega_I)$ is 1.217%. For the box inclusion, the relative error becomes 4.55%. The mass of the box is not concentrated around a point but is more spread along the radial direction. In this case a two-parameter approximation by a ring becomes questionable. However, even in this case the representation error is smaller than the modelling error, see Section 4.4 of [1]. As before, all the parameters are the same as by Figure 4(c), except a and b ,

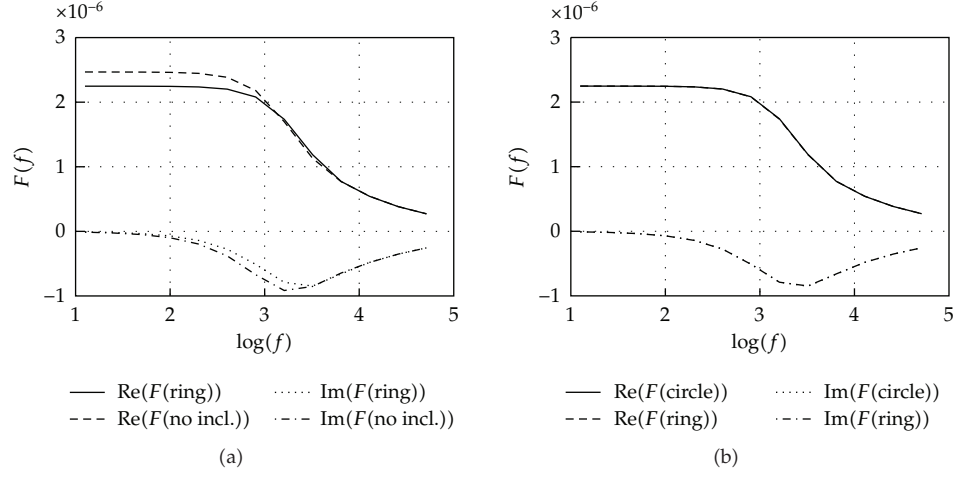


Figure 5: Accuracy of 1D model for circular inclusion; 0.724% relative error of $F(\omega)$ between 1D and 2D model for $f \in [2, 2^{14}]$.

which are computed so that the masses of the object and of the corresponding ring are equal and that $(a + b)/2$ coincide with the center of mass of the object.

3. One-Dimensional Inverse Problem

In the previous section, we have shown that quite general inclusions can be reasonably well approximated by a ring inclusion. It means if one has real world data, these can be described by a very simple explicitly solvable model (2.3)–(2.7) with only two-parameters a and b . In the case of two disjunct inclusions, we could consider two rings. Let us suppose that a, b are unknown parameters, that is, we do not know if there is an inclusion and if yes where the inclusion is buried. We study the following inverse problem.

Problem 1. Determine constants a and b in (2.3)–(2.7), that is, determine the ring inclusion, based on measurements of $F(\omega, R_I)$ for different frequencies ω .

$F(\omega, R_I)$ given by (2.1) can be computed explicitly, see [10]. We obtain

$$\begin{aligned}
 F(\omega, R_I) &= \int_0^{2\pi} \int_0^c r \mu H(r) = 2\pi \int_0^c r \mu H(r) \\
 &\stackrel{(2.8)}{=} 2\pi \left\{ \mu^h c_1 \int_0^a r J_0(kr) + \int_a^b r \mu_0 H_I + \mu^h \int_b^c r [c_2 J_0(kr) + c_3 K_0(-ikr)] \right\} \quad (3.1) \\
 &= 2\pi \left(\mu^h c_1 \frac{a J_1(ka)}{k} + \mu_0 H_I \frac{b^2 - a^2}{2} + \mu^h \left[c_2 \frac{r J_1(kr)}{k} - c_3 \frac{r K_1(-ikr)}{-ik} \right]_b^c \right).
 \end{aligned}$$

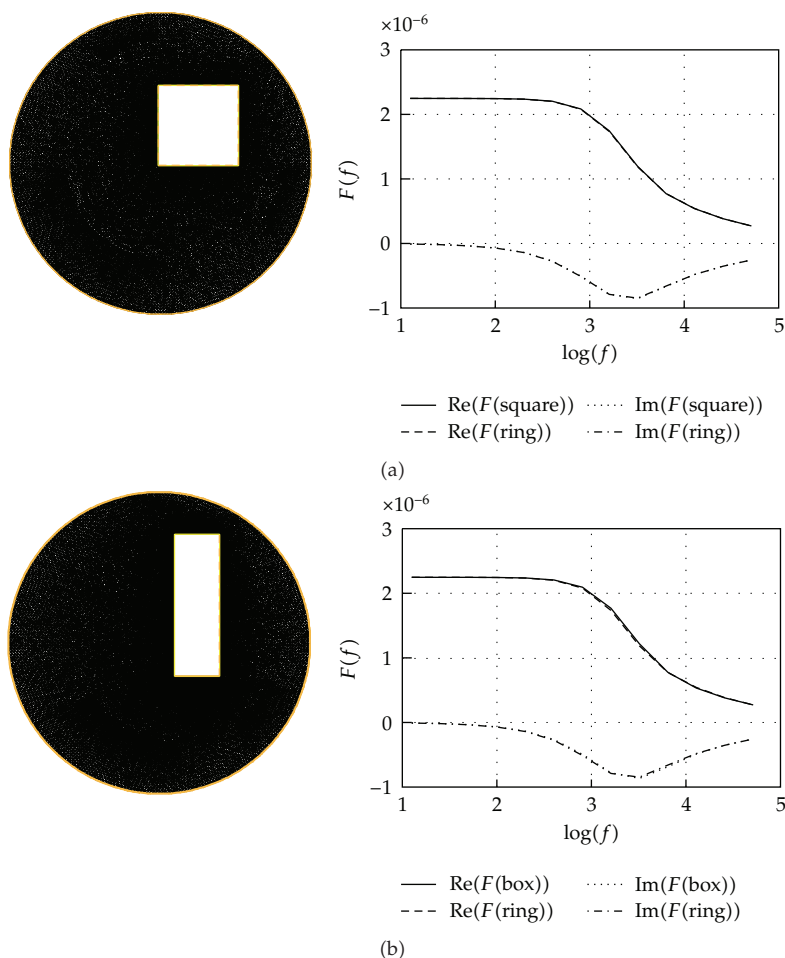


Figure 6: Fingerprints of 1D model for (a) square inclusion -1.217% relative error of $F(\omega)$; (b) box inclusion -4.55% relative error of $F(\omega)$.

3.1. Uniqueness

Theorem 3.1. *The ring inclusion, that is, $a \in \mathbb{R}$, $b \in \mathbb{R}$, such that $a > 0$, $c > b > a$ can be uniquely determined by two measurements of $\Re(F(\omega, R_I))$ for $\omega = 0$ and for $\omega = \epsilon$, where ϵ is sufficiently small.*

Proof. The proof is quite technical, but the main idea is simple. The area $S = |R_I|$ of the ring inclusion is uniquely determined by a single measurement for $\omega = 0$. Thus it is sufficient to obtain the uniqueness for one of the parameters a , b , say a . Then $b = \sqrt{S/\pi + a^2}$. Consequently we can consider $F(\omega, R_I)$ to be a function of a only. We would like to show that if $\Re(F(\omega, a = a_1)) = \Re(F(\omega, a = a_2))$ for an $\omega > 0$, then $a_1 = a_2$. This seems to be, working directly with Bessel functions, quite difficult.

The idea is to exploit the asymptotic behaviour of Bessel functions when $\omega \rightarrow 0$. We consider the Taylor expansion of $F(\omega, a)$ with respect to ω at $\omega = 0$, that is,

$$F(\omega, a) = F(0, a) + \frac{\partial F(0, a)}{\partial \omega} \omega + \mathcal{O}(\omega^2). \quad (3.2)$$

The $F(\omega, a)$ is an analytic function in ω , since it is an integral of a linear combination of Bessel functions, which are analytical (except for the origin in the case of K_0) [10]. The coefficients $c_i, i = 0, \dots, 2$ of the linear combination are dependent on ω via (2.7), but are also analytical. We can indeed use (3.2).

Now, we evaluate $F(0, a)$ and $\partial F(0, a)/\partial \omega$ from (3.2). We obtain immediately that

$$F(0, a) = H_E \left[\mu_0 |S| + \mu (\pi c^2 - S) \right] \quad (3.3)$$

since $\lim_{\omega \rightarrow 0} H = H_E$. To evaluate $\partial F(0, a)/\partial \omega$ we employ the asymptotic behaviour of Bessel functions. We have

$$\begin{aligned} \lim_{x \rightarrow 0} n! \left(\frac{2}{x} \right)^n J_n(x) &= 1, \quad n = 0, \dots, \\ \lim_{x \rightarrow 0} \left(-\ln \left(\frac{x}{2} \right) \right)^{-1} K_0(x) &= 1, \\ \lim_{x \rightarrow 0} x K_1(x) &= 1. \end{aligned} \quad (3.4)$$

The solution H to (2.3)–(2.7) can be expressed as $H = H_1 + \alpha H_2 + \beta H_3$ where $H_i, i = 1, \dots, 3$, are the solutions to the following problems

$$\begin{aligned} \frac{1}{r} \frac{dH_1}{dr} + \frac{d^2 H_1}{dr^2} &= i\omega \sigma^h \mu^h H_1, \quad \text{in } \Omega_C, \\ H_1(c) &= H_E, \\ H_1(a) = H_1(b) &= 0, \\ \frac{dH_1}{dr}(0) &= 0, \\ \frac{1}{r} \frac{dH_2}{dr} + \frac{d^2 H_2}{dr^2} &= i\omega \sigma^h \mu^h H_2, \quad \text{in } \Omega_C, \\ H_2(c) &= 0, \\ H_2(a) = H_2(b) &= 1, \\ \frac{dH_2}{dr}(0) &= 0, \\ \frac{1}{r} \frac{dH_3}{dr} + \frac{d^2 H_3}{dr^2} &= i\omega \sigma^h \mu^h H_3, \quad \text{in } \Omega_C, \\ H_3(c) &= 0, \\ H_3(a) = H_3(b) &= i, \\ \frac{dH_3}{dr}(0) &= 0. \end{aligned} \quad (3.5)$$

α and β are determined by (2.7). Using this, (3.1) can be alternatively expressed as

$$F(\omega, a) = 2\pi\mu \left\{ \int_0^c r H_1(r) + \alpha(\omega, a) \int_0^c r H_2(r) + \beta(\omega, a) \int_0^c r H_3(r) \right\}. \quad (3.6)$$

We differentiate the right-hand side of (3.6) with respect to a and take the limit for $\omega \rightarrow 0$. By a tedious computation we obtain

$$\frac{\partial \Re(F(0, a))}{\partial \omega} = \lim_{\omega \rightarrow 0^+} \frac{\partial \Re(F(\omega, a))}{\partial \omega} = \pi H_E \mu \frac{2c^2 \ln(c/b) + b^2 - c^2}{2 \ln(c/b)}. \quad (3.7)$$

Let us differentiate (3.2) with respect to a . We obtain

$$\frac{\partial \Re(F(\omega, a))}{\partial a} = \frac{\partial \Re(F(0, a))}{\partial a} + \frac{\partial}{\partial a} \left(\frac{\partial \Re(F(0, a))}{\partial \omega} \right) \omega + \mathcal{O}(\omega^2), \quad (3.8)$$

where we employ (3.3) and (3.7) and obtain

$$\frac{\partial \Re(F(\omega, a))}{\partial a} = \pi H_E \mu a \frac{2b^2 \ln(c/b) + b^2 - c^2}{2 \ln^2(c/b) b^2} \omega + \mathcal{O}(\omega^2). \quad (3.9)$$

We obtained that for ω small enough we can approximate $\partial \Re(F(\omega, a))/\partial a$ by a simple expression. This expression is always negative, since $2b^2 \ln(c/b) + b^2 - c^2$ is always negative for $b < c$. To see this just we use substitution $x = b/c$. We obtain

$$2b^2 \ln\left(\frac{c}{b}\right) + b^2 - c^2 = c^2 (-2 \ln(x) + x^2 - 1), \quad (3.10)$$

where $-2 \ln(x) + x^2 - 1$ is negative for $x < 1$. We obtained that $\Re(F(\omega, a))$ is decreasing in a , which gives the uniqueness. \square

Remark 3.2. One of the parameters in the above proof is identified on the basis of the measurement at zero frequency. Let us note, that the second one could be roughly identified using the skin depth

$$\rho = \sqrt{\frac{2}{\omega \sigma \mu}} \quad (3.11)$$

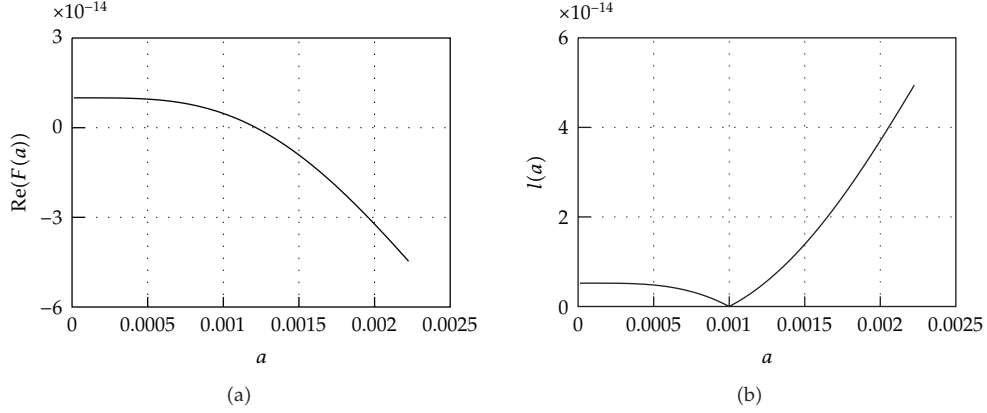


Figure 7: (a) plot of F for $f = 0.1$ Hz as a function of a shifted by $-1.97885562 \cdot 10^{-6}$ (b) the corresponding $l(a)$ (optimal $a = 0.0010$ m, $b = 0.0015$ m).

as long as a defect much deeper than ρ cannot be detected. The higher the frequency, the smaller the skin depth. We have the following estimates based on the asymptotic expansions of Bessel functions of a very large argument (see, e.g., [10]):

$$\begin{aligned} |J_\nu(z)| &\leq \left| (2 + \alpha) \left(\frac{2}{\pi z} \right)^{1/2} \right|, \\ |K_\nu(z)| &\leq \left| (1 + \alpha) \left(\frac{\pi}{2z} \right)^{1/2} e^{-z} \right|, \end{aligned} \quad (3.12)$$

where $\nu \in \mathbb{R}$ is the order of the Bessel function, α is any positive real number and $|z|$ is sufficiently large. Thus we have that H , given by (2.8), relatively quickly drops in amplitude. The parameter k in the argument of the Bessel function in (2.8) is inversely proportional to the skin depth: $|k| = \sqrt{2}\rho^{-1}$. Consequently, when using a sufficiently high angular frequency ω , skin depth ρ is small, the field penetrate not deep enough and we are not able to see a difference in the flux F for a cable with and without an inclusion as long as this inclusion is buried much deeper than ρ . This can be observed in Figure 5.

To confirm numerically Theorem 3.1 we computed $F(\omega, a)$ for small $f = 0.1$ Hz. The inclusion is given by $a = 0.0010$ m and $b = 0.0015$ m. $F(\omega, a)$, depicted in Figure 7(a), is indeed a decreasing function of a . Let us define a least square problem by the following functional:

$$l(a) := \sum_{i=0}^n \left(\Re(F(\omega_i, a)) - \tilde{F}_i \right)^2, \quad (3.13)$$

where $\tilde{F}_i, i = 1, \dots, n$, are measurements of the real part of the magnetic induction through the cross section of the cable for different frequencies $f_i, i = 1, \dots, n$. In Figure 7(b) we depicted $l(a)$ corresponding to $F(\omega, a)$ of Figure 7(a). We have two exact measurements for $f_0 = 0$ Hz and $f_1 = 0.1$ Hz, that is, $n = 2$. We see that $l(a)$ really achieves its minimum at $a = 0.0010$ m.

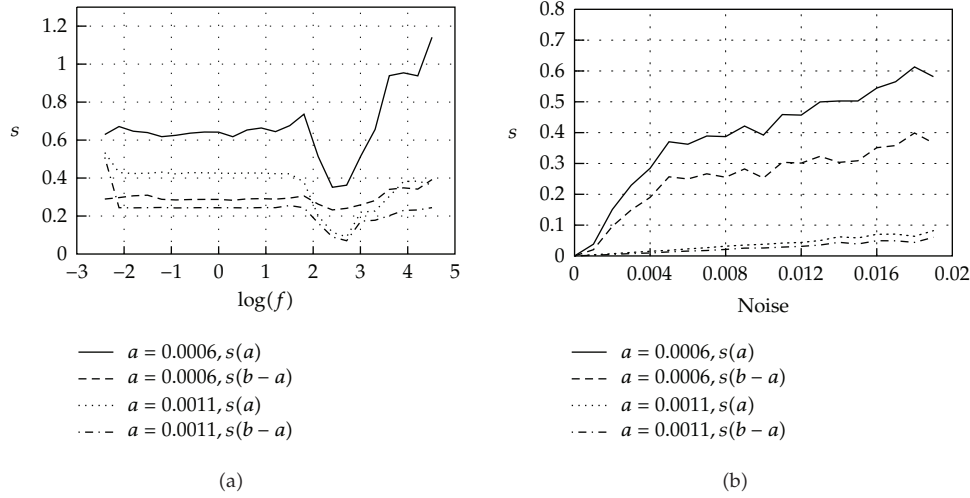


Figure 8: Sensitivity of parameters a and $b - a$ in the case of two measurements to: (a) frequency choice f_1 ($f_0 = 0$ Hz), (b) noise; $c = 0.0025$ m, $b - a = 0.0005$ m in all experiments; in (a) noise is 1%; in (b) $f_1 = 500$ Hz.

3.2. Stability Analysis

Relation (3.9) from the proof of Theorem 3.1 could be used to analyze the sensitivity of Problem 1 for very low frequencies. But since the problem is ill-posed, one usually tries to sample for a very broad range of frequencies to ensure stability. We will analyze the stability of Problem 1 numerically.

To calculate a and b on the basis of measurements we use a hybrid minimization algorithm. First we run a global search on a rough grid. Then we employ the Levenberg-Marquardt [11, 12] algorithm to find the local minimum. We implemented the problem in C++ using [13]. The global search on a rough grid is computationally feasible since the evaluation of the explicit function (3.1) takes only approximately 0.3 ms on a regular PC (Intel Core2 Duo CPU T7250 @ 2.00 GHz).

First, we will consider only two measurements, one for $f_0 = 0$ Hz and one for a variable frequency f_1 . We want to see how the choice of f_1 influences the accuracy. We consider uniform distributed noise of 1%. In the global search we take a uniformly distributed grid of 20×20 points. The maximum number of iterations for the Levenberg-Marquardt algorithm is set to 100. We compute the relative standard deviation s for samples of $N = 1000$ computations, that is, for example for a

$$s = \sqrt{\frac{\sum_1^N (a_i - a)^2}{a^2 N}}, \quad (3.14)$$

where a is the known value (not average) and $a_i, i = 1, \dots, N$, are the sampled values.

The results are depicted in Figure 8(a). We consider two gaps $a = 0.0006$ m and $a = 0.0011$ m with the same width $b - a = 0.0005$ m.

The first observation is that only the measurements for a quite narrow interval of frequencies yield the best possible accuracy. The second observation is that for two measurements with 1% level of noise s never falls under 5% level, that is, two measurements are

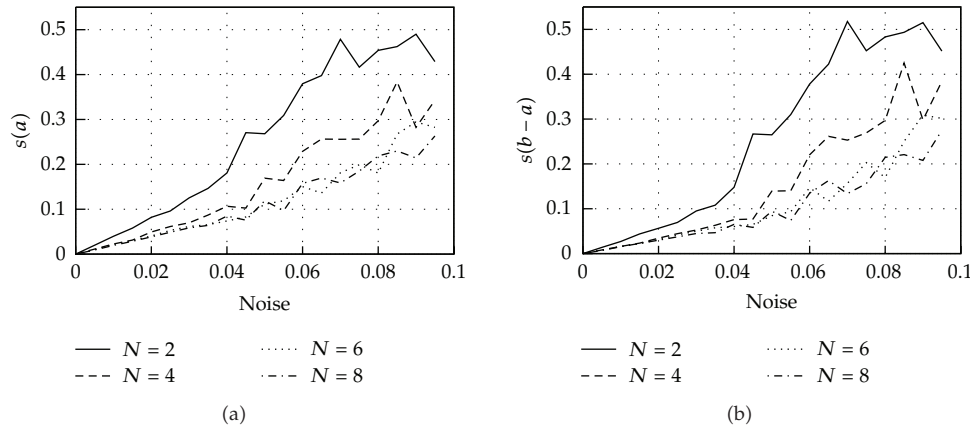


Figure 9: Standard deviation of parameters $a = 0.0011$ and $b - a = 0.0005$ (as a function of noise) for different numbers of measurements ($N = 2, 4, 6, 8$): (a) $s(a)$; (b) $s(b - a)$.

certainly not enough. And the third observation is that the inclusions buried deeper inside, that is, $a = 0.0006$ m, are recovered less accurately than the inclusions close to the surface.

Now, let us take a fixed frequency $f = 500$ Hz, which lies in the optimal interval according to the above experiment. We consider the sensitivity of the inverse problem with two measurements for different levels of noise. The global search is performed on a uniformly distributed grid of 50×50 points. The relative standard deviation s for recovered parameters, computed for samples of $N = 100$, is depicted in Figure 8(b). The results again confirm that the inclusions buried deep inside are much more sensitive to the noise in the measurements than those close to the surface. Even for very low levels of noise is the accuracy of the recovery of a deep buried inclusion quite poor.

Let us analyze how the number of measurements influences the accuracy. We considered $N = 2, 4, 6, 8$ measurements where $f_0 = 0$ Hz in all the cases and $f_i = 500 + 100(i - N/2)$ Hz, $i = 1, \dots, N - 1$, that is, the measurements are regularly distributed around “optimal” value $f = 500$ Hz. We again sample 100 times and we also take a uniformly distributed grid 50×50 for the global search as before. Figure 9 depicts standard deviations s of a and of $b - a$ for different numbers of measurements as a function of noise. Considering more measurements improves the accuracy significantly. For $N = 8$ and the noise level of 5% which is our expected modeling error, see Section 4.3 of [1], $s(a)$ is around 10% and $s(b - a)$ even drops under 10%. Slightly better accuracy for $b - a$ with respect to a is due to the fact that $b - a$ is computed based on all the measurements, but the position a is indifferent to the measurement $f_0 = 0$ Hz.

Figure 10 depicts the averages \bar{a} and $\overline{b - a}$. Let us recall we sample 100 times. The error of recovery lies for $N = 8$ within 10% error band for both \bar{a} and $\overline{b - a}$. Notice, that the corresponding $s(a)$ and $s(b - a)$ are around 0.3. We see that the averages \bar{a} and $\overline{b - a}$ are biased estimators of a and $b - a$, respectively. We assume that the reason is of algorithmic nature.

4. Real Data Experiment

We present a real case study to confirm the usefulness of the proposed inclusion detection method.

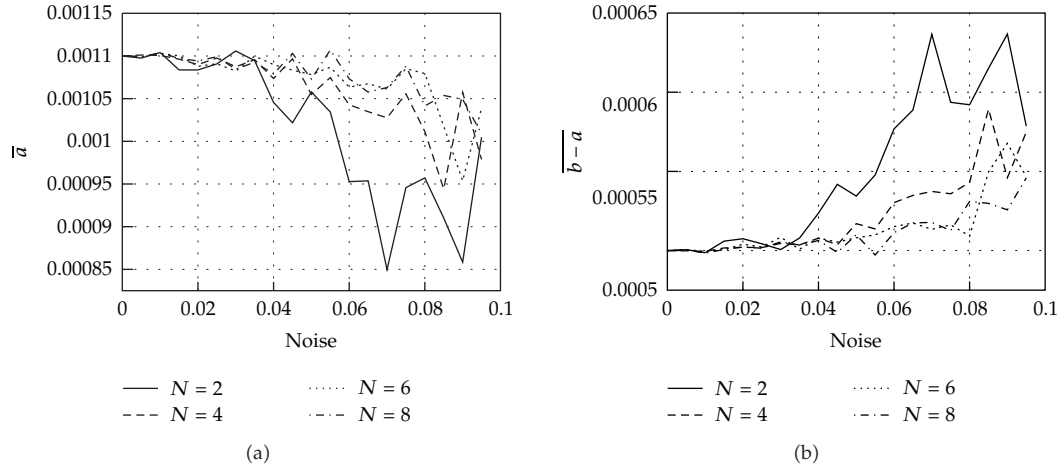


Figure 10: Average values of parameters $a = 0.0011$ m and $b - a = 0.0005$ m (as a function of noise) for different numbers of measurements ($N = 2, 4, 6, 8$): (a) \bar{a} ; (b) $\overline{b - a}$.

4.1. Experiments

The experimental setup is identical to the setup from [1]. The considered cable has 7 bundles of strands, each bundle consists of 19 wires with a diameter of 0.3 mm: Figure 1(a). The inspection of the cross section of the cable shows that the center s of all bundles except the central one is situated at a radial distance of approximately 1.6 mm.

To obtain measurements for validating the model, three ring core sensors for hysteresis loops were made by winding an excitation and a measurement winding around the material to test.

- (i) For the first ring core, the material to test is a set of 18 strands that were electrically insulated by giving them an acryl coating.
- (ii) For the second ring core, the material to test is a piece of undamaged coated cable: Figure 1(c).
- (iii) For the third ring core, the material to test is the same cable where one bundle of strands is removed over 10 mm length: Figure 1(d).

To make the ring cores, firstly the strands (for the first ring core) or the cable (for the second and the third ring core) were folded to a ring (toroid) with 300 mm circumference. A ferrite core was added around the connection of the cable ends to close the magnetic lines. This simulates an infinitely long cable. Then, an excitation and a measurement winding were added, uniformly distributed along the circumference. Finally, an isolating tape was added: see Figures 1(c) and 1(d).

Let us note that it is also possible to make a straight sensor that can be moved over a cable to continuously scan new sections of a long cable.

We measured on each ring core on the one hand 40 quasistatic BH -loops (0.5 Hz) between 0 and 5150 A/m, and on the other hand dynamic BH -loops and corresponding losses for four levels of magnetic induction (50 mT, 100 mT, 200 mT, 500 mT) and for frequencies f of 50, 100, 200, 300, 500, 1000, 2000, 3000, and 5000 Hz. Generating the current for the excitation winding is done by a National Instruments PCI-6110 data acquisition card

in combination with a Kepco 50 V/8 A linear amplifier. The voltage waveform induced in the measurement coil—proportional to $d\phi/dt$ —is integrated via an analog integrator. For each induction level and for each frequency, this integrated waveform obtained from the measurement coil is sampled simultaneously with the enforced current waveform in the excitation coil. The sampling is done by the same data acquisition card at a sampling rate of 200 samples per period for the loops at 3 and 5 kHz, and at a rate of 1000 samples per period for the other frequencies (0.05 to 2 Megasamples per second). In the LabVIEW software, the integrated waveform of the measurement coil is converted to an induction waveform $B(t)$ and the current waveform is converted to the externally applied field waveform $H(t)$ via Ampère's law. This results in the dynamic BH hysteresis loops, used by the inverse problem. The LabVIEW program has a feedback control algorithm on the waveform shape of the induction: it adjusts the excitation current waveform in order to obtain a sinusoidal induction waveform.

4.2. Identification of the Parameters for the Homogenized Models

The homogenized models used in the inverse problem, see Section 4.3, require the homogenized permeability μ^h , and the homogenized conductivity σ^h .

The homogenized permeability is a function of the magnetic induction. It is found via quasistatic (0.5 Hz) hysteresis loop measurements on ring core 1, that consists of individually isolated strands. The modelling of the hysteresis loops is done using a complex magnetic permeability. In a time harmonic model, this complex permeability produces ellipses in the BH -plane. The determination of the complex permeability for a given frequency and amplitude is done by a least squares fitting of the ellipses on the measured quasistatic hysteresis loops. Evidently, the ellipses are only an approximation of the experimental hysteresis loops: the deviation between the ellipses and the measured loops is small if the material is not saturated (Figure 11(a)); the shape of the experimental hysteresis loops deviates more from the fitted ellipses if the material is saturated (Figure 11(b)). Once the complex permeability is found for a broad range of induction values, the homogenized permeability is found using the homogenization result—Theorem 3.1 in [1]. We obtained $\mu^h(50 \text{ mT}) = (8.43799 \cdot 10^{-5}, -9.72202 \cdot 10^{-6})$, $\mu^h(100 \text{ mT}) = (0.00010495, -2.79189 \cdot 10^{-5})$, $\mu^h(200 \text{ mT}) = (0.000160883, -9.77414 \cdot 10^{-5})$, and $\mu^h(500 \text{ mT}) = (0.000318907, -0.00028671)$.

The homogenized conductivity σ^h is found for each of the models via an inverse problem with as input the measured dynamic loops on ring core 2 (the cable without an inclusion), as explained in [1]. See Section 4.3 for the values of σ^h for a particular model from that section.

The physical electrical conductivity (not the homogenized conductivity σ^h) is found to be 4.1 MS/m by enforcing a DC current in a strand and by measuring the voltage over a well-known length of the strand.

4.3. Identification of Defects by Solving the Inverse Problem

In [1] we derived three successive versions of the homogenized model. All the models incorporate magnetic hysteresis via the complex homogenized permeability μ^h .

In the case of *Model 1*, σ^h is a real function of the induction level. *Model 2* considers σ^h to be a complex function of the induction level. Consequently, it can describe electric hysteresis effects as well. The most accurate model, *Model 3*, assumes that σ^h is a complex function

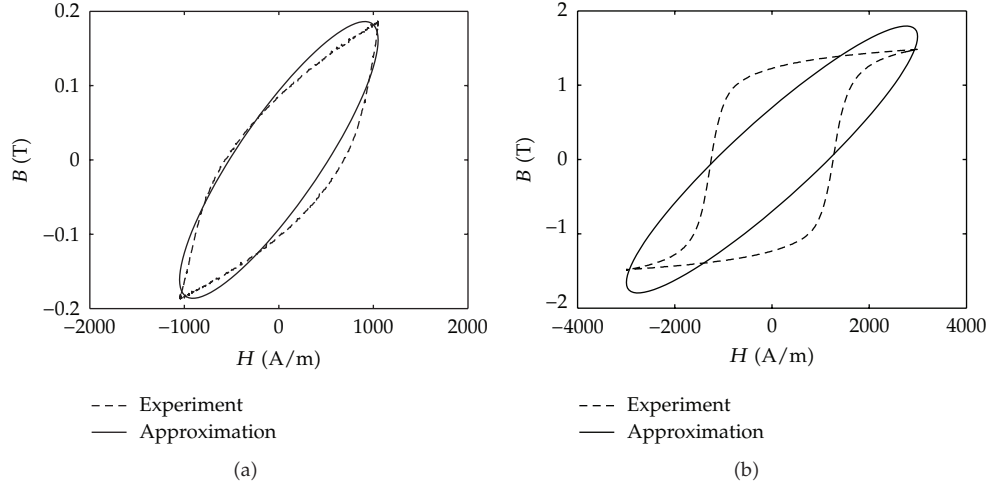


Figure 11: (a) Quasi-static BH -loops (0.5 Hz) for $H \approx 1000$ A/m and $B \approx 0.2$ T is a good approximation of the measured loop; (b) ellipse for $H \approx 3000$ A/m and $B \approx 1.5$ T is a worse approximation.

Table 1: Fitted homogenized conductivity of *Model 1*.

| Induction (mT) | σ^h (S/m) | Relative error |
|----------------|------------------|----------------|
| 50 | 20808 | 15.24% |
| 100 | 28585 | 14.94% |
| 200 | 83014 | 17.99% |
| 500 | 274716 | 19.43% |

of frequency, particularly that $\sigma^h = \sigma_1^h + \omega\sigma_2^h$, where σ_1^h and σ_2^h are only functions of the induction level. The models achieve accuracies around 15%, 10%, and 5%, respectively. In Tables 1, 2, and 3 we present the homogenized σ^h for all the models as obtained in [1]. The achieved modeling errors are therein presented as well.

We test how the models can comply with a real data inclusion detection problem described above. The results are summarized in Table 4. Two numbers are presented:

- (i) N —the number of wires detected defined by

$$N := \frac{\pi(b^2 - a^2)}{(\pi 0.00015^2)\chi}, \quad (4.1)$$

where 0.00015 m is the radius of the small wire and χ is the fill factor, that is, how much from the cable area is occupied by the wires. We have

$$\chi = 7 \cdot 19 \cdot \frac{\pi 0.00015^2}{\pi 0.0025^2} = 0.4788, \quad (4.2)$$

- (ii) s —the center of the ring, that is, $s = (a + b)/2$.

We expect that the optimal values are approximately $N = 19$ and $s = 1.6$ mm. Each row of Table 4 represents a different set of measurements which is taken into account.

Table 2: Fitted complex homogenized conductivity of *Model 2*.

| Induction (mT) | $\text{Re}(\sigma^h)$ (S/m) | $\text{Im}(\sigma^h)$ (S/m) | Relative error |
|----------------|-----------------------------|-----------------------------|----------------|
| 50 | 30410 | -73968 | 8.66% |
| 100 | 34044 | -56107 | 8.22% |
| 200 | 86895 | -116639 | 9.80% |
| 500 | 333436 | -187726 | 14.33% |

Table 3: Fitted complex homogenized conductivity of *Model 3*.

| Induction (mT) | $\text{Re}(\sigma_1^h)$ (S/m) | $\text{Im}(\sigma_1^h)$ (S/m) | $\text{Re}(\sigma_2^h)$ (S/m) | $\text{Im}(\sigma_2^h)$ (S/m) | Relative error |
|----------------|-------------------------------|-------------------------------|-------------------------------|-------------------------------|----------------|
| 50 | 49411 | -155675 | -0.213612 | 0.944442 | 5.76% |
| 100 | 58097 | -112239 | -0.284609 | 0.654771 | 5.04% |
| 200 | 173886 | -174930 | -2.33445 | 1.7578 | 5.98% |
| 500 | 512867 | -151052 | -14.3317 | -0.206326 | 8.90% |

Table 4: Real experiment; N : the number of detected wires; s : the center of the ring; (a) all measurements; (b) low frequencies: all measurements for $f \in [0.5, 300]$ Hz; (c) middle frequencies: all measurements for $f \in [100, 1000]$ Hz; (d) high frequencies: all measurements for $f \in [500, 5000]$ Hz.

| <i>Model</i> → | 1 | | 2 | | 3 | |
|----------------|-------|----------|-------|----------|-------|----------|
| Sample ↓ | N | s [mm] | N | s (mm) | N | s (mm) |
| (a) | 23.03 | 1.5979 | 17.90 | 1.5897 | 11.82 | 1.9204 |
| (b) | 17.80 | 2.3876 | 16.09 | 2.3989 | 11.60 | 2.4213 |
| (c) | 24.83 | 2.3698 | 22.39 | 2.3900 | 16.38 | 1.9177 |
| (d) | 42.35 | 0.7179 | 24.47 | 0.5750 | 13.26 | 1.2940 |

We have altogether 40 measurements for 4 different induction levels. We consider all the measurements ($N = 40$), low frequency measurements for $f \in [0.5, 300]$ Hz ($N = 20$), middle frequencies for $f \in [100, 1000]$ Hz ($N = 20$) and only the high frequency measurements for $f \in [500, 5000]$ Hz ($N = 20$).

From the results of the first two models, that is, *Model 1* and *Model 2*, we conclude that the measurements for the complete spectrum of frequencies have to be included to obtain accurate results. Taking all the measurements yields very good agreement with the expected values. *Model 1* found that 23.03 small wires were removed from the radial position $r = 1.5979$ mm. *Model 2* found that 17.90 small wires were removed from the radial position $r = 1.5897$ mm. There is very good agreement of the recovery between the models, especially of the position.

Model 2 recovers the number of removed wires more accurately. It suggests that this model is better in predicting low frequency behaviour of the problem. The low frequencies (magnetic effects) are responsible for accurate recovery of the removed mass.

The results of the most accurate *Model 3* are not consistent even for the whole set of the measurements, see Table 4(a). Based on the good results of the other two models, we can conclude that there are two possible reasons for the behaviour. First, probably 4 parameters per induction level are too many to fit. Let us note, the problem of finding σ_1^h and σ_2^h is ill-posed. A sufficient number of measurements and/or some kind of regularization are needed to get feasible σ_1^h and σ_2^h . Second, the results of the model from Figure 10 in [1] show that the

losses are not monotonically decreasing, which we think is not physical. One probably has to enforce some constraints on σ_1^h and σ_2^h to correct the model.

5. Conclusions

We considered a problem of detection of inclusions in a metallic cable using a homogenized model derived in [1] and global magnetic hysteresis loops measurements for both low and high frequency (up to 5000 Hz).

We reduced the original 2D problem to a one-dimensional problem by symmetrization of a possible inclusion to a ring. We showed numerically that this reduction is rather accurate with respect to the flux through the cross section. At the same time, the inclusion is described by only two-parameters. The resulting 1D model has a piecewise analytical solution, which allowed us to evaluate explicitly the flux through the cross section of the cable. Thus the model is very fast.

We studied an inverse problem of detection of the ring inclusion. We obtained a uniqueness result, studied sensibility and considered a real data experiment.

The results show that—despite of its simplicity—the model is applicable in real world conditions. The most accurate adaptation of the model achieves an accuracy around 5% when estimating the number of defect strands and the radial position of the defect.

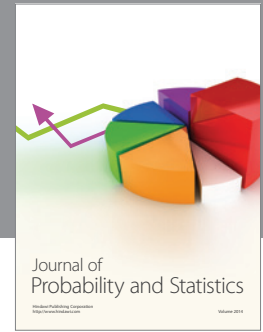
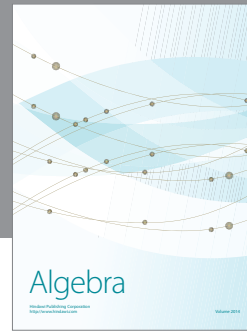
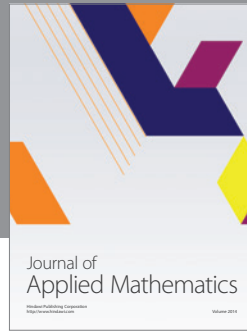
Acknowledgments

Valdemar Melicher would like to acknowledge the support of IAP-P6/21-project “Inverse problems and optimization in low frequency electromagnetism” and of BOF doctor-assistant research mandate 01P09209T of Ghent University, Ghent, Belgium. Peter Sergeant is supported by the Fund for Scientific Research—Flanders FWO, Belgium.

References

- [1] V. Melicher and P. Sergeant, “Homogenized eddy current model for non-destructive testing of metallic cables,” submitted.
- [2] G. Tian, Z. Zhao, and R. Baines, “The research of inhomogeneity in eddy current sensors,” *Sensors and Actuators A*, vol. 69, pp. 148–151, 1998.
- [3] E. Cardelli, A. Faba, R. Specogna, A. Tamburrino, F. Trevisan, and S. Ventre, “Analysis methodologies and experimental benchmarks for eddy current testing,” *IEEE Transactions on Magnetics*, vol. 41, no. 5, pp. 1380–1383, 2005.
- [4] Y. Li, T. Theodoulidis, and G. Y. Tian, “Magnetic field-based eddy-current modeling for multilayered specimens,” *IEEE Transactions on Magnetics*, vol. 43, no. 11, pp. 4010–4015, 2007.
- [5] V. Cacciatore, A. Canova, A. Vallan, and B. Vusini, “Experience and technologies in ndt of ropes,” in *Proceedings of the 7th International Conference on Damage Assessment of Structures (Damas '07)*, L. Garibaldi, C. Surace, K. Holford, and W. Ostachowicz, Eds., vol. 347 of *Engineering Materials*, Trans Tech Publications, Torino, Italy, 2007.
- [6] A. Canova and B. Vusini, “Magnetic analysis of non-destructive testing detectors for ferromagnetic ropes,” *The International Journal for Computation and Mathematics in Electrical and Electronic Engineering*, vol. 27, no. 4, pp. 869–878, 2008.
- [7] V. Isakov, *Inverse Problems for Partial Differential Equations*, vol. 127 of *Applied Mathematical Sciences*, Springer, New York, NY, USA, 1998.
- [8] K. Sungwhan and Y. Masahiro, “Uniqueness in the two-dimensional inverse conductivity problems of determining convex polygonal supports: case of variable conductivity,” *Inverse Problems*, vol. 20, no. 2, pp. 495–506, 2004.

- [9] A. Abou-Elyazied Abdallah, P. Sergeant, G. Crevecoeur, L. Vandenbossche, and L. Dupre, "Magnetic material identification in geometries with non uniform electromagnetic fields using global and local magnetic measurements," *IEEE Transactions on Magnetics*, vol. 45, pp. 4157–4160, 2009.
- [10] G. N. Watson, *A Treatise on the Theory of Bessel Functions*, Cambridge University Press, London, UK, 1922.
- [11] K. Levenberg, "A method for the solution of certain non-linear problems in least squares," *Quarterly of Applied Mathematics*, vol. 2, pp. 164–168, 1944.
- [12] D. W. Marquardt, "An algorithm for least-squares estimation of nonlinear parameters," *Journal of the Society for Industrial and Applied Mathematics*, vol. 11, pp. 431–441, 1963.
- [13] M. Lourakis, "levmar: Levenberg-marquardt nonlinear least squares algorithms in C/C++," 2004, <http://www.ics.forth.gr/~lourakis/levmar/>.



Hindawi

Submit your manuscripts at
<http://www.hindawi.com>

